An improved radiative forcing scheme for better representation of Arctic under-ice blooms

Yuexin Gao [a,b], Yang Zhang [b,*], Fei Chai [b], Mats A. Granskog [c], Pedro Duarte [c], Philipp Assmy [c]

[a] *College of Oceanography, Hohai University, Nanjing, China*
[b] *State Key Laboratory of Satellite Ocean Environment Dynamics, Second Institute of Oceanography, Ministry of Natural Resources, Hangzhou, China*
[c] *Norwegian Polar Institute, Fram Centre, Tromsø, Norway*

ARTICLE INFO

ABSTRACT

In the present study, a newly designed radiative forcing scheme, i.e., impulsive radiative forcing scheme (IRFS), is applied in the one-dimensional Regional Ocean Modeling System-Carbon Silicate Nitrate Ecosystem (ROMS-CoSiNE) model to reproduce under-ice phytoplankton blooms (UIBs) in the Arctic Ocean. The model results obtained with the IRFS and the traditional continuous radiative forcing scheme (CRFS) are compared with observations of an UIB north of Svalbard. It is found that, the new IRFS performs much better than the traditional CRFS with lower biases, lower root-mean-square difference (RMSD), and a higher correlation coefficient (r), especially at the near-surface layer of the water column (0–15 m). It is also found that in the simulations with the CRFS, the UIB started earlier and maximum chlorophyll concentration was more than twice the observed data. However, the UIB with the IRFS is similar to observations in terms of UIB timing and magnitude. Since the IRFS allows more solar radiation to penetrate through the upper water column, phytoplankton growth is supported at greater water depth (10–40 m). Therefore, this model reproduces a deeper phytoplankton bloom and corresponding deepened subsurface chlorophyll maxima, which agrees well with the observations. Additionally, the introduction of melt ponds into the IRFS model plays a vital role in accelerating spring UIBs because ponded ice can transmit more light. However, the magnitude of integrated chlorophyll-a hardly changes between the model runs with and without melt ponds. This study proposes a more accurate averaging of the light field that simply changes the averaging procedure to take into account horizontal light variability at the sub-grid scale and provides an approach to improve radiative forcing scheme in the Pan-Arctic model case.

1. Introduction

In recent decades, the Arctic Ocean has experienced rapid changes in sea ice extent and thickness, with old, stable multi-year ice being largely replaced by young, thinner first-year ice (Maslanik et al., 2011; Stroeve et al., 2012; King et al., 2018). According to the National Snow and Ice Data Center (NSIDC) records, the sea ice extent in the Arctic showed a clear downward trend from 1978 to 2020 and reached its lowest level on record in September 2012 (https://nsidc.org/arcticseaicenews/). Recently, under-ice phytoplankton blooms (UIBs) were widely observed in the Arctic (Mundy et al., 2009, 2014; Arrigo et al., 2012; Assmy et al., 2017; Oziel et al., 2019) as a result of sea ice thinning (Kwok and Rothrock, 2009; Polyakov et al., 2012; Horvat et al., 2017) and increased melt pond fraction (Rösel et al., 2012; Clement Kinney et al., 2020). The thinning sea ice and increasing melt pond coverage increases light transmission to the

underlying water column that initializes UIBs (Frey et al., 2011; Arrigo et al., 2012; Palmer et al., 2014; Zhang et al., 2015; Ardyna et al., 2020a,b). Additionally, sea ice melting and water column stratification in spring contribute to driving bloom dynamics (Lowry et al., 2018). Accordingly, UIBs have been widely observed across the Arctic Ocean, which may challenge the previous paradigms of Arctic-wide production that under-ice phytoplankton production can be negligible due to the strong light attenuation of sea ice and snow (Arrigo and van Dijken, 2015; Ardyna et al., 2020a,b; Payne et al., 2021). Massive UIBs can generate ecological consequences as they enhance the Arctic Ocean's under-ice productivity (Arrigo et al., 2014; Clement Kinney et al., 2020). However, UIBs may consume nutrients and thus limit pelagic phytoplankton growth in open waters after sea ice retreating (Jin et al., 2016). Therefore, changes in the total primary production in the Arctic Ocean may or may not be correlated directly to sea ice changes, depending on nutrient availability (Jin et al., 2016).

* Correspondence to: State Key Laboratory of Satellite Ocean Environment Dynamics, Second Institute of Oceanography, MNR, 36 North Baochu Road, Hangzhou, China.
E-mail address: yzhang@sio.org.cn (Y. Zhang).

Although UIBs are critical to Arctic production, studies are limited due to sporadic observations limited by the harsh environment at high latitudes (Lee et al., 2016; Clement Kinney et al., 2020). Also, current satellite-based estimates of high-latitude annual primary production are confirmed to be underestimated by an order of magnitude, because satellites cannot detect phytoplankton beneath sea ice (Arrigo et al., 2012, 2014). Thus, to bridge this gap, physical–biogeochemical models are important tools for understanding the ecosystem processes in the Arctic Ocean and for revealing their regulating factors (Jin et al., 2006; Horvat et al., 2017). It is worth mentioning that multiple numerical pelagic biogeochemical models have been used successfully to study the Arctic Ocean planktonic ecosystems in various spatial/temporal scales (e.g., Slagstad and Støle-Hansen, 1991; Walsh et al., 2004; Lavoie et al., 2009; Zhang et al., 2010, 2015; Mortenson et al., 2017; Schourup-Kristensen et al., 2018). The significance of under-ice productivity has been confirmed by many model studies, in which the under-ice production contributes about one third of the Arctic total production (Popova et al., 2010; Jin et al., 2016; Schourup-Kristensen et al., 2018). Based on the three-dimensional (3D) Biology/Ice/Ocean Modeling and Assimilation System (BIOMAS), Zhang et al. (2015) showed that the area fraction of UIBs in the Arctic increased in response to the increasing light availability and nutrient availability in the upper 100 m of the ocean during 1988–2013. However, compared to the particulate organic carbon concentrations observed by the Impacts of Climate on Ecosystems and Chemistry of the Arctic Pacific Environment (ICESCAPE) program, BIOMAS model's results were inconsistent in simulating the UIB's depth and subsurface chlorophyll maxima (SCM). According to the model experiments of Palmer et al. (2014) on varying melt pond coverage, there was no phytoplankton growth beneath the ice until the melt pond fraction increased to 10%. The regional annual net primary production in the 0% pond run was 4.7% lower than the result of the 30% pond run. However, compared with the increasing trend in melt pond fraction, the thinning of sea ice is more significant to increase the bloom potential in the Arctic (Horvat et al., 2017). Lavoie et al. (2009) indicated that the snow/ice cover melt and/or ice break-up control(s) the phytoplankton bloom timing, and the bloom's magnitude is nutrient-limited. Additionally, in terms of the community structure, in the model study of Slagstad and Støle-Hansen (1991), it was shown that except for the diatoms that dominated the bloom, *Phaeocystis* also contribute to the nitrate exhaustion in the upper 30 m of the water column in the Barents Sea. A simple primary production model described by Assmy et al. (2017) also studied the growth potential of *Phaeocystis* under the sea ice cover north of Svalbard. The model reproduced the considerable increase of *Phaeocystis* beneath the sea ice cover during the N-ICE2015 expedition from May to June 2015. However, the model neglected effects of nutrient limitation, grazing, and non-grazing mortality.

Previous studies have indicated that solar radiation is important for biogeochemical simulations in high latitude regions, and the light attenuation by sea ice plays an important role in calculating under-ice radiation (Laufkötter et al., 2015; Lee et al., 2016; Simo-Matchim et al., 2017; Schourup-Kristensen et al., 2018). In the literature, e.g., Palmer et al. (2014), Zhang et al. (2015), Mortenson et al. (2017), and Stroeve et al. (2021), the common radiative forcing scheme is based on the area-weighted average method (Castellani et al., 2022), which was originally defined by Perovich (2005). However, because of the heterogeneous distribution of sea ice and the relative movement between ice and the underlying water column, solar radiation penetrating into the water column may not be horizontally homogeneous. It may imply large spatial fluctuations in a sub-grid scale as the water column alternates among different surface conditions (Hill et al., 2018; Lowry et al., 2018; Massicotte et al., 2019; Ardyna et al., 2020b). As a result, the area-weighted average radiation scheme may generate misestimation of phytoplankton growth because of the nonlinear relationship between phytoplankton growth with light (Slagstad and Støle-Hansen, 1991; Hill et al., 2018). Consequently, the magnitude of UIBs may
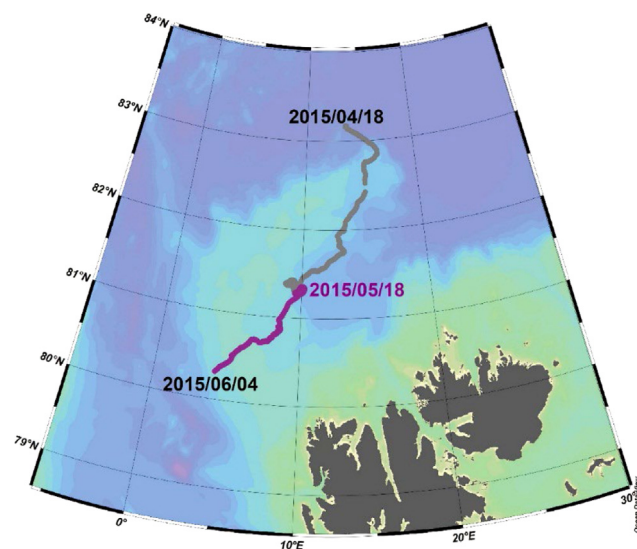

Fig. 1. Drift tracks of the N-ICE2015 Floe 3 (gray) and the model (purple).

also be misestimated in models (Zhang et al., 2015; Mortenson et al., 2017). Although several studies suggested that improvements could be achieved by using higher spatial resolution models, allowing to better capture the heterogeneity of light penetration (Popova et al., 2010; Schourup-Kristensen et al., 2018, 2021), it is still hard to reproduce all aspects of the locally small scale (<1 km) sea ice features, such as melt ponds and leads (Wang et al., 2016; Massicotte et al., 2019). Therefore, the present study designs a new radiative forcing scheme to offset the simulation biases caused by the traditional radiative forcing scheme.

The main motivation of this study is to design and deploy a new radiative forcing scheme in a one-dimensional (1D) physical–biogeochemical coupled model to improve the model's ability in reproducing the UIB observed north of Svalbard during the Norwegian young sea ICE expedition (N-ICE2015). The rest of the paper is structured as follows. In Section 2, the numerical model and the two radiative forcing schemes are described. In Section 3, the model results are compared with the observed data during the drift of N-ICE2015 Floe 3, and based on the results, the differences between the two radiative forcing schemes and the regulating factors that drive UIBs are discussed. Finally, in Section 4, some conclusions are provided.

2. Materials and methods

2.1. Description of the N-ICE2015 expedition

The N-ICE2015 expedition with the vessel *Lance frozen* in the Arctic ice pack provided a research platform for interdisciplinary investigation in the high Arctic (Granskog et al., 2016). During this expedition, a *Phaeocystis*-dominated UIB in the Arctic Ocean was captured (Assmy et al., 2017; Ardyna et al., 2020a,b). This UIB was encountered over the Yermak Plateau north of Svalbard during the drift of Floe 3 from May to early June 2015 (Fig. 1; Granskog et al., 2018). Analyses of the local currents and the Chl-a concentrations in this area implied that the bloom grew in-situ beneath the ice pack. The almost unchanged silicate concentration in the upper 50 m during the bloom period suggested that no substantial diatom growth had taken place in this area (Assmy et al., 2017). Leads in the ice pack were frequently created by ice divergence events prior to the bloom period (Itkin et al., 2017), which is characteristic of the ice pack north of Svalbard (Willmes and Heinemann, 2016). Mixed layer depth shallowed dramatically after May 25th, from an average of 64 m to an average of 6 m (Meyer et al., 2017), and the water column was highly stratified when the bloom took place (Assmy et al., 2017). The UIB coincided with pycnocline
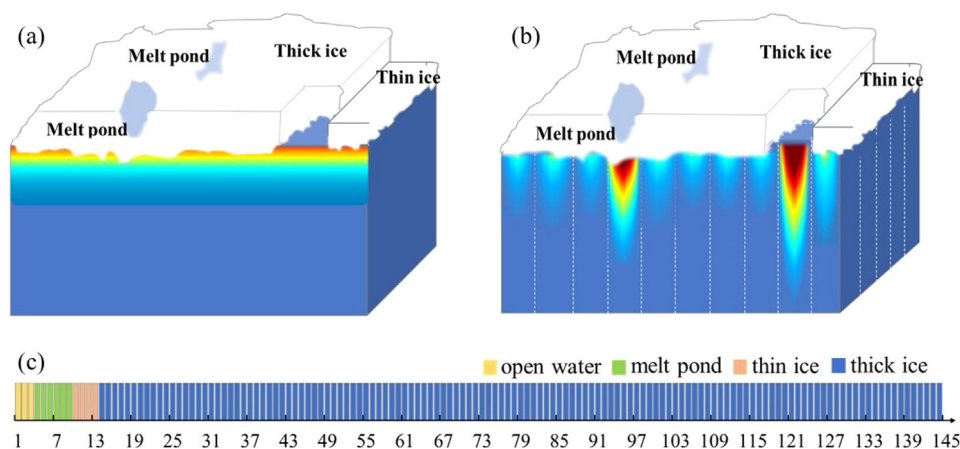
Fig. 2. Conceptual diagrams representing (a) the water column in the continuous radiative forcing scheme (CRFS) and (b) the sub-columns in the impulsive radiative forcing scheme (IRFS) drifting with the overlying pack ice with multiple surface types, (c) an example of how the surface types distributed in a fixed sequence over a diurnal cycle, in which the fractions of thick ice, thin ice, melt ponds, and open water are 0.91, 0.03, 0.04, and 0.02, respectively. Note: Contour plots in (a) and (b) represent the PAR distribution in the water column.

shallowing and a high refrozen lead fraction which provided favorable conditions for the UIB development even below sea ice covered with thick snow (Assmy et al., 2017). The surface nitrate inventory was nearly depleted from 10.37 to 1.42 μmol L^{-1} due to the consumption by phytoplankton and small vertical nitrate flux caused by the strong upper ocean stratification during the bloom period (Randelhoff et al., 2016; Assmy et al., 2017). N-ICE2015 provided novel interdisciplinary data from the high Arctic (Granskog et al., 2018). These data will be used to improve model initialization, parameterization, climatological nudging, and validation.

2.2. General description of the 1D model

This study is based on a 1D version of the 3D physical–biogeochemical coupled Regional Ocean Modeling System-Carbon Silicate Nitrate Ecosystem (ROMS-CoSiNE) model (Xiu and Chai, 2011). In this model, the biogeochemical model is based on the CoSiNE model developed by Chai et al. (2002) and is modified to contain 15 state variables, including:

(1) Seven dissolved matters, i.e., nitrate (NO_3), ammonium (NH_4), silicate ($Si(OH)_4$), phosphate (PO_4), dissolved oxygen (DO), dissolved inorganic carbon (TCO_2), and total alkalinity (TALK);
(2) Two kinds of particles, i.e., particulate organic nitrogen (PON) and biogenic silica (bSi).
(3) Two phytoplankton types, i.e., non-diatoms (P1, mainly *Phaeocystis* in the present study) and diatoms (P2), and the corresponding chlorophyll (Chl-a1 and Chl-a2) of these phytoplankton components;
(4) Two grazer types, i.e., microzooplankton (Z1) and mesozooplankton (Z2).

Note that all the above variables are described in detail in Chai et al. (2002) and Xiu and Chai (2011, 2014). Table B.2 provides a list of parameters used in the model and their units and values.

2.3. Model setup and data sources

The 1D ROMS-CoSiNE model is set to run under a Lagrangian coordinate, implying that the position of the 1D model drifts along with the drift of Floe 3 of the N-ICE2015 expedition (Fig. 1; Granskog et al., 2018). The model is run at a time-step of 600 s, and the model's largest depth is fixed to 991.7 m. The vertical coordinate is divided into 100 layers with the resolution varies from 0.58 m at the sea surface to 28.1 m at the bottom layer. The simulation is

initialized with the observed profiles of temperature, salinity, nitrate, silicate, phosphate, ammonium, phytoplankton, and corresponding Chl-a (Assmy et al., 2016) on May 18th before the UIB started. By fixing the known variables to the initial conditions and forcing of May 18th, the model is spun up for three model years to reach a steady state to derive the initial biomass of the two zooplankton groups and the initial value of other state variables, i.e., DO, PON, bSi, TCO_2, TALK, which cannot be obtained from the observations directly. To make the physical environment realistic, in this model, the water temperature and salinity are assimilated daily from observations (Dodd et al., 2016). The European Centre for Medium-Range Weather Forecasts (ECMWF) reanalysis data (ERA-5) is used to produce the hourly atmospheric forcing, including air temperature, surface pressure, relative humidity, shortwave radiation, net longwave radiation, wind speed, and precipitation.

Moreover, extensive field data of snow and sea ice thickness from Floe 3 of the N-ICE2015 expedition (Rösel et al., 2017) are used to calculate the mean thicknesses of different types of sea ice. Measured incident and transmitted photosynthetically available radiation (PAR) data are used to calculate the sea ice extinction coefficients (Taskjelle et al., 2016). The areal fractions of thick ice, thin ice, and open water are taken from Assmy et al. (2017). The fraction of melt ponds is from the multi-year average of the melt pond data provided by the Integrated Climate Data Center (ICDC, http://icdc.zmaw.de, Rösel et al., 2012; Istomina et al., 2015).

2.4. Definition of two different radiative forcing schemes

In the present study, a new radiative forcing scheme is designed and used in the 1D ROMS-CoSiNE model. The traditional radiative forcing scheme is also adopted by the model for comparison. As shown in Fig. 2a and b, we assume the pack ice over the water column is a mix of four sea surface types (thick ice, thin ice, melt ponds, open water), and they are classified as:

(1) Thick ice: sea ice thickness larger than 28 cm with snow cover larger than 5 cm, representing large areas of thick ice in the region;
(2) Thin ice: sea ice thickness less than or equal to 28 cm with snow cover less than or equal to 5 cm;
(3) Melt ponds;
(4) Open water.
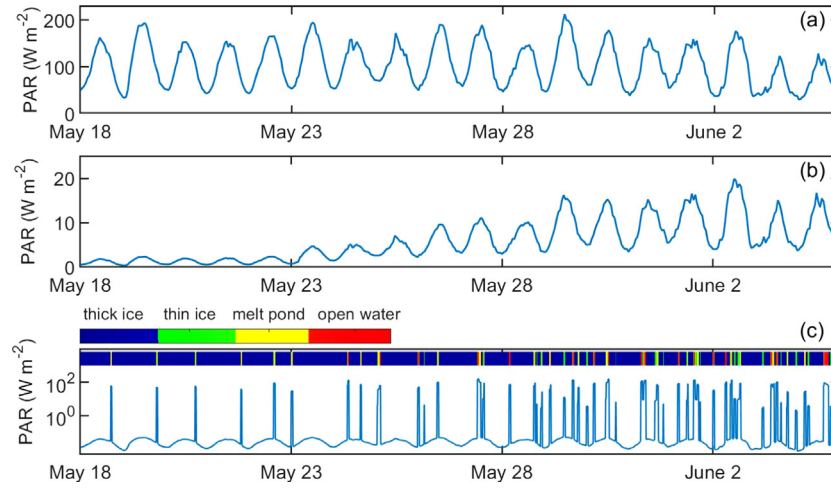
Fig. 3. (a) Incident surface PAR (W m^{-2}), and simulated PAR (W m^{-2}) at the sea water surface (at surface in open water or right below ice for other cases) with (b) the CRFS and (c) the IRFS. Note: Colored area at the top of (c) represents the surface types at that time, and this is an example for one of the sub-columns in the IRFS.

We suppose this spatially heterogeneous pack ice drifts along with the underlying water column although there are relative motions between them. Accordingly, two different radiative forcing schemes are established as:

(1) Continuous radiative forcing scheme (CRFS): This scheme was extensively used in previous studies (e.g., Palmer et al., 2014; Zhang et al., 2015; Assmy et al., 2017; Mortenson et al., 2017; Castellani et al., 2022). In this scheme, the water column is treated as a whole (Fig. 2a) and the PAR at the ice–ocean interface is derived by Eq. (1) as the weighted mean of transmitted PAR for all surface conditions ($\overline{PAR_s}$). As shown in Fig. 3b, the PAR time series at the sea water surface shows a continuous and smooth sinusoidal wave shape. Thus, hereafter, this radiative scheme is called the continuous radiative forcing scheme. In this scheme, phytoplankton growth (G_{con}) at each time-step is calculated as:

$$\overline{PAR_s} = \sum_{i=1}^{n} \left(PARs_i \cdot fice_i \right), \tag{1}$$

$$G_{con} = f(T, \overline{PAR_s}, N), \tag{2}$$

where $PARs_i$ stands for the PAR under each type of surface conditions (i), namely thick/thin/ponded ice and open water, $n = 4$ stands for the different surface conditions considered in the model and $fice_i$ stands for the areal fraction of different surface types. Since the variations of sea surface types are provided daily, $fice_i$ are fixed in a diurnal cycle. Also, T and N represent the temperature and nutrients, respectively.

(2) Impulsive radiative forcing scheme (IRFS): In this scheme, we divide the underlying water column into several isolated sub-columns and each of them can only be covered by one sea surface type at a time-step (Fig. 2b). Given that there are relative motions between the spatially heterogeneous ice pack and the underlying water column, the model assumes a 144-time steps (24 h divided by 600 s time interval) diurnal cycle with alternating periods of sea ice, melt ponds, and open water. Note that the time-steps occupied by a certain surface type in one day is derived by its areal fraction ($fice_i$) in that day. For example, 1 for thick ice is simulated as a diurnal cycle with 144 time-steps of thick ice and zero steps of other surface types, while the fractions of 0.91, 0.03, 0.04, and 0.02 for thick ice, thin ice, melt ponds, and open water respectively are simulated as a diurnal cycle with 133 time-steps of thick ice, 4 time-steps of thin ice, 6 time-steps of melt ponds, and 3 time-steps of open water (Fig. 2c). In this condition, for each sub-column, the sea surface PAR value tends to have an impulsive shape with a higher value during open water or melt ponds and lower value under the ice-covered conditions (Fig. 3c). Thus, it is called the impulsive radiative forcing scheme. Phytoplankton growth (G_{imp}) at each time-step of is calculated as:

$$G_{imp} = f(T, PARs_i, N). \tag{3}$$

Table 1
Differences between the model cases. CRFS: continuous radiative forcing scheme, IRFS: impulsive radiative forcing scheme.

	Radiative forcing scheme	Melt ponds
Case 1	CRFS	Included
Case 2	IRFS	Included
Case 3	IRFS	Excluded

In contrast with the CRFS, G_{imp} at each time-step is calculated with one surface condition (thick/thin/ponded ice or open water) in this model. This scheme converts the spatial sea ice variability into temporal sequences changes and attempts to reproduce the "realistic conditions" in which a water column experiences different surface types in a diurnal cycle. In the present study, in view of the spatial heterogeneity of the surface, the water column is divided into 50 small sub-columns (Fig. 2b). These sub-columns are simulated in independent model runs and their diurnal sequences of four types of surface conditions are random. Finally, when the 50 model runs are finished, we calculate the ensemble mean of these simulation results as the final result of this scheme. The ensemble mean represents the mean condition of the water column, and is comparable with the traditional CRFS.

Furthermore, melt ponds on sea ice strongly reduce the surface albedo and the extinction effect, enhancing light transmission to the underlying water column (Rösel et al., 2012). Therefore, in order to examine the model performance with the two radiative forcing schemes and the impact of melt ponds, we configure three comparison cases as shown in Table 1. Cases 1 and 2 are used to examine the model improvement due to the new radiative forcing scheme. Case 3 is used to examine the modulating effect of melt ponds on the UIBs.

2.5. Transmission of incident PAR through sea ice and the water column

We use hourly shortwave radiation from ECMWF to simulate the daily light cycle in the model. There is only part of the spectrum (400−700 nm) relevant for biological processes (Arrigo et al., 2014; Castellani et al., 2022), which is termed PAR. Therefore, the PAR to shortwave radiation ratio of 0.43 is used to determine the incident PAR on the snow/ice surface (PAR_{in}, in unit W m^{-2}; Zhang et al., 2010; Frants et al., 2020). To calculate the intensity of sea surface PAR (PAR_s), the procedure of Light et al. (2008) and Duarte et al. (2015) is followed:

$$PAR_s = PAR_{in} \cdot \left(1 - Alb_s \right) \cdot \exp \left(-k_s \cdot Z_s \right) \cdot I0_{ice} \cdot \exp \left(-k_{ice} \cdot Z_{ice} \right), \tag{4}$$

where Alb_s is the snow surface albedo, k_s and k_{ice} are extinction coefficients of snow and ice, respectively. Also, $I0_{ice}$ denotes the fraction

of radiation transmitting through the highly scattering surface of the ice, and Z_s and Z_{ice} are snow and sea ice thicknesses, respectively. It should be noted that extensive field surveys confirmed that snow/ice thicknesses for thick/thin ice did not change significantly during the drift of Floe 3. Thus, although fractions of four types of surface condition vary, the mean snow/ice thicknesses for thick/thin ice are constant during the simulation period. The mean value of thin ice thickness is 25 cm with the snow cover of 5 cm, and the mean value of thick ice thickness is 149 cm with the snow cover of 45 cm. Following Assmy et al. (2017), the coefficients used in Eq. (4) are adjusted using the N-ICE2015 dataset (Taskjelle et al., 2016). For thick ice with thick snow, some of the parameters in Eq. (4), including Alb_s, $I0_{ice}$, and k_{ice}, are from previous studies (Light et al., 2008; Taskjelle et al., 2017). Also, Z_s and Z_{ice}, the mean thickness of thick snow and thick ice, are 45 cm and 149 cm, respectively. k_s for thick snow is derived based on the measured incident and transmitted PAR (Taskjelle et al., 2016), and its value is 10.69 m^{-1}. Similarly, for thin ice with thin snow, transmittance measurements for snow ice and bare ice were done in the N-ICE2015 expedition. According to these measurements and the known parameters (Alb_s and $I0_{ice}$; Light et al., 2008), the extinction for thin bare ice can be estimated as 3.25 m^{-1}. Subsequently, k_s for thin snow (8.98 m^{-1}) is estimated from the transmittance measurements with snow cover. For melt ponds, the Alb_s, $I0_{ice}$, and k_{ice} are 0.251, 0.645, and 0.99, respectively (Light et al., 2008; see specific parameters in Table B.2). In the water column, light attenuation is calculated as a function of water column depth and Chl-a concentration (Chai et al., 2002; Xiu and Chai, 2014):

$$PAR_{(z)} = PAR_s \cdot \exp\left\{-k_1 z - k_2 \int_{-z}^{0} (\text{Chl} - \text{a1} + \text{Chl} - \text{a2})dz\right\}, \quad (5)$$

where k_1 is the light attenuation due to seawater (0.046 m^{-1}), and k_2 is the light attenuation due to phytoplankton (0.03 m^{-1}).

3. Results and discussion

3.1. Overall comparison of the two radiative forcing schemes

The simulation results show that all of the independent model runs with IRFS for the 50 sub-columns can reproduce the main features of the observed UIB, including the SCM structure from late May to early June in 2015 (the ensemble mean of these 50 model runs will be shown later). The upper 50 m averaged Chl-a of these 50 model runs are convergent with a mean standard deviation of 0.092 (Fig. 4a and b). Thus, it implies that the diurnal sequence of different surface types does not significantly affect the simulation results, mainly due to the relatively small light variability and the large predominance of one ice type over the others during the simulation period. Based on the observation–simulation match-up Chl-a, the Taylor diagram (Fig. 4a) with normalized standard deviation (SD), the root-mean-square difference (RMSD) and correlation coefficient (r) shows that the simulation results estimated by the IRFS has a smaller SD (0.96) and RMSD (0.67) than those estimated by the CRFS with values of 1.76 and 1.36, respectively. The values also show that the model runs with the IRFS have better model–observed correlation relationship with a mean value of 0.76 than the CRFS with a correlation coefficient of 0.64.

To quantitatively compare the CRFS and IRFS cases, the upper 50 m of the water column is divided into two layers by the mean mixed layer depth of 15 m during the bloom development. Comparisons between the observed and simulated Chl-a concentrations for the depth range 0–50 m and in both layers mentioned above are shown in Fig. 5. For the upper 50 m, Chl-a is obviously overestimated by the CRFS case with a bias of 1.79 mg m^{-3}, while it is slightly underestimated by the IRFS case with a bias of −0.04 mg m^{-3} (Fig. 5a). This can also be seen in Fig. 4b, in which the CRFS result shows a higher peak than the IRFS result. Fig. 5b shows an obvious overestimation of Chl-a within the depth of 0–15 m simulated by the CRFS case with a bias of 3.34 mg m^{-3}. In

contrast, the bias of the IRFS case is −0.42 mg m^{-3}. Moreover, the IRFS case has higher model–observed correlation and smaller RMSD than CRFS case at 0–15 m (Fig. 5b). For the layer at 16–50 m, the biases of IRFS and CRFS cases are 0.21 and 0.81, respectively, and their r values are equal (Fig. 5c). The higher RMSD of the CRFS case (5.46) indicates that for this depth range, simulated Chl-a does not match observations very well.

3.2. Bloom process comparison of two radiative forcing scheme models

As the sea ice concentration decline from May 23rd, for the CRFS model case, $\overline{PAR_s}$ increases accordingly, and for the IRFS case, the period with high-light exposure extends. The daily-average sea surface PAR processes are shown in Fig. 6a and b. For both model cases, daily PAR value increases from May 23rd, and phytoplankton Chl-a increases correspondingly (Fig. 6a–f). It implies that the impacts of increasing light penetrations on the initialization of rapid growth in under-ice phytoplankton. Consequently, nitrate is depleted to nearly zero from the surface to a depth of around 10 m for the continuous radiative case and to a depth of around 18 m for the IRFS case (Fig. 6g and h).

For the CRFS case, Chl-a remains close to initial values for only a short time (2 days) and then increases rapidly on May 23rd, exceeding the UIB threshold of 2.5 mg m^{-3} (Lowry et al., 2014). This increase occurs much earlier than the beginning of the observed UIB (Fig. 6e). The simulated maximum Chl-a concentration is 17.1 mg m^{-3}, which is more than twice the observed peak value (7.5 mg m^{-3}). Moreover, PAR is attenuated rapidly in the water column, resulting in a euphotic depth of 22.4 m during the bloom (Fig. 6c). As a result, rapid phytoplankton growth is mainly confined to the surface layer, leading to a significant vertical gradient of Chl-a across the euphotic depth during the bloom (Fig. 6e).

For the IRFS case, the intermittent appearance of melt ponds and open water weakens the light attenuation due to snow/ice, which allows PAR to transmit to the deep layer intermittently (Fig. 6d). Consequently, the Chl-a distribution for the IRFS case is more homogeneous than the CRFS case in the vertical direction, and the euphotic zone in the IRFS is averaged of 43.0 m during the bloom, which is comparable with previous study in the similar area with similar environmental conditions (Massicotte et al., 2019). Moreover, the comparisons of Chl-a between observation and simulation results show that the IRFS case can better reproduce the UIB development than the CRFS case. Chl-a in the water column covered by the sea ice remains close to initial value (<1 mg m^{-3}) until thick ice reduces and the open water fraction starts to build-up on May 24th. Phytoplankton bloom starts on May 24th, and then the bloom forms with Chl-a greater than 2.5 mg m^{-3} between 0–30 m by May 26th with the increasing light transmission (Fig. 6f). Over the next three days, the bloom keeps on developing and peaks at 7.3 mg Chl-a m^{-3} in late May. Then, the UIB migrates downward following the nutricline, forms a SCM of 7.3–8.6 mg Chl-a m^{-3} at depth range of 11–31 m, and deepens as time passes. It is also worth mentioning that this modeled SCM is consistent with the observational pattern in terms of depth and magnitude (Fig. 6f).

3.3. Phytoplankton types

Simulated Chl-a concentrations of non-diatoms and diatoms in the upper 50 m of the water column are shown in Fig. 7a and b. Note that the UIB is dominated by non-diatoms. Diatoms' contribution is less than 2.2% of total Chl-a, although a diatom increase is modeled between 30–50 m by the end of the simulation period (Fig. 7b). It is worth mentioning that this result is supported by the observational phytoplankton taxonomy data, which shows that *Phaeocystis* accounted for 55%–92% of phytoplankton abundance. Also, during the bloom period, silicate was almost unconsumed, suggesting that there was no substantial diatom growth during the observational period (Assmy et al., 2017). Diatom dominated UIBs have been frequently reported
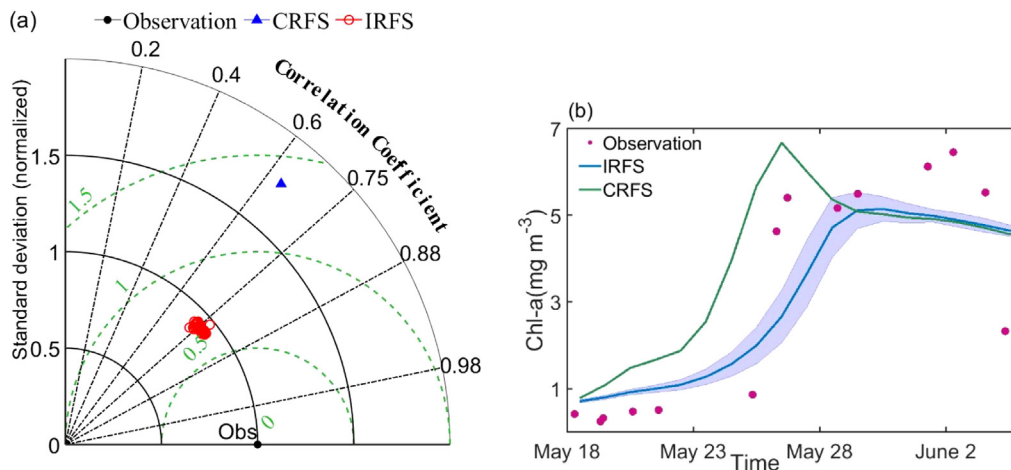
Fig. 4. (a) Taylor diagram of the normalized standard deviation (meridional direction, 1 denotes the closest to observation), correlation coefficient (zonal direction, 1 denotes the best correlation between model and observation), and RMSD (the contour lines, the smaller the better) of the observation-simulation match-up Chl-a, (b) comparison of the averaged Chl-a in the upper 50 m between model runs with the CRFS and IRFS (shaded area represents 3-fold standard deviations) and observations.
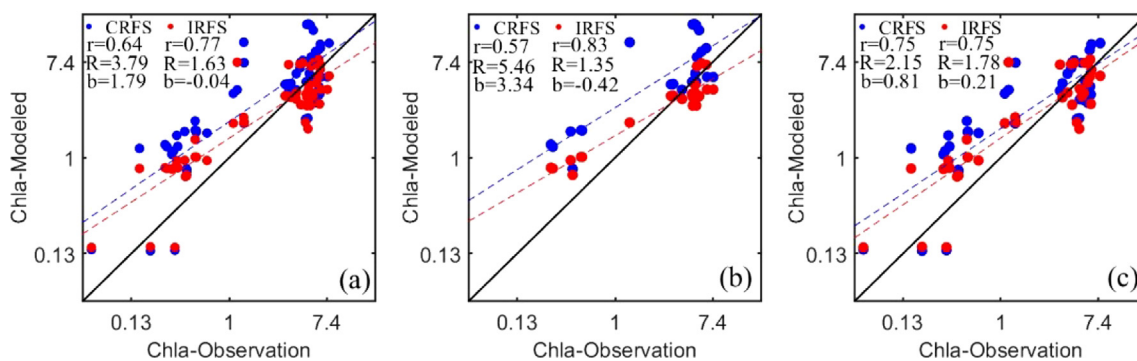

Fig. 5. Comparisons of simulated Chl-a with observations at the layers of (a) 0–50 m, (b) 0–15 m, and (c) 16–50 m. Note: The black solid lines indicate equality and the dashed lines represent the best fit to the observations.

from the Arctic Ocean (Mundy et al., 2009; Degerlund and Eilertsen, 2010; Arrigo et al., 2012; Hill et al., 2018; Johnsen et al., 2018). However, the UIB observed during the N-ICE2015 expedition is the first *Phaeocystis* dominated UIB (Assmy et al., 2017; Ardyna et al., 2020b). *Phaeocystis* cells are possibly carried from lower latitudes to this area at greater depths by the Atlantic water and then are mixed upwards to the upper ocean by the storm events in an earlier time of the year (Assmy et al., 2017), leading to a higher *Phaeocystis* concentration than diatoms in the initiation of the simulation. The low light conditions beneath the snow-covered drifting pack ice are apparently insufficient to sustain a diatom bloom in early spring. *Phaeocystis* are generally more competitive than diatoms in low light environment, helping to maintain its dominance in the simulations (Sakshaug et al., 2009; Johnsen et al., 2018). Note that the photosynthetic parameterization of our model is from the onboard experiment (Cota et al., 1994; Assmy et al., 2017) and *Phaeocystis*' dominance can also be seen in the model results. Moreover, the low silicate inventory with the molar ratio of nitrogen to silicon (N/Si) much larger than 1.0 in this area limits diatom dominance (Ardyna et al., 2020b). As the surface silicate does not change significantly, the N/Si ratio remains far higher than 1.0 until nitrate is nearly depleted by the UIB at the end of May (Figs. 6h and 7c). This is quite different from the western Arctic Ocean where the water masses are influenced by Pacific-derived waters with higher silicate concentrations. Thus, the dominant phytoplankton species in the Pacific sector are represented by diatoms (Ardyna et al., 2020a).

3.4. Growth limitation

Phytoplankton growth can be limited by temperature, nutrients, and light (Andersen, 1989; Smith and Sakshaug, 1990; Gosselin et al., 1997; Hill and Cota, 2005; Lee and Whitledge, 2005; Campbell et al., 2009). Among the growth limiting factors, light and nutrients are the decisive terms for Arctic UIBs (Popova et al., 2010; Lewis et al., 2018). Since the *Phaeocystis* is the overwhelming dominant group in the N-ICE2015 UIB, light and nitrogen limitations and net growth of *Phaeocystis* for both CRFS and IRFS cases are analyzed and the results are shown in Fig. 8. The limitation indices of light and nitrogen are calculated as:

$$L_{lim} = \left[1 - \exp(\frac{-\alpha PAR}{\mu_{max}}) \right] \exp(\frac{-\beta PAR}{\mu_{max}}), \qquad (6)$$

$$N_{lim} = \frac{NO_3}{(k_{no3} + NO_3)} \cdot e^{-\varphi_1 NH_4} + \frac{NH_4}{(k_{nh4} + NH_4)}, \qquad (7)$$

where L_{lim} and N_{lim} represent the limitation indices of light and nitrogen, respectively. For every limitation index, high value indicates less limitation. Also, α is the initial slope of the photosynthesis-irradiance curve, β is the photoinhibition term; μ_{max} is the maximum growth rate, k_{no3} and k_{nh4} represent the half-saturation constant for nitrate and ammonium, and φ_1 is the NH_4 inhibition parameter. Values and units of all these parameters are shown in Table B.2.

For the IRFS case, following the thick ice decline, the light limitation index increases rapidly from near zero to above 0.2 in the surface water from May 23rd (Fig. 8a). For the CRFS case, the light limitation index is higher than 0.1 immediately after the simulation starts and increases
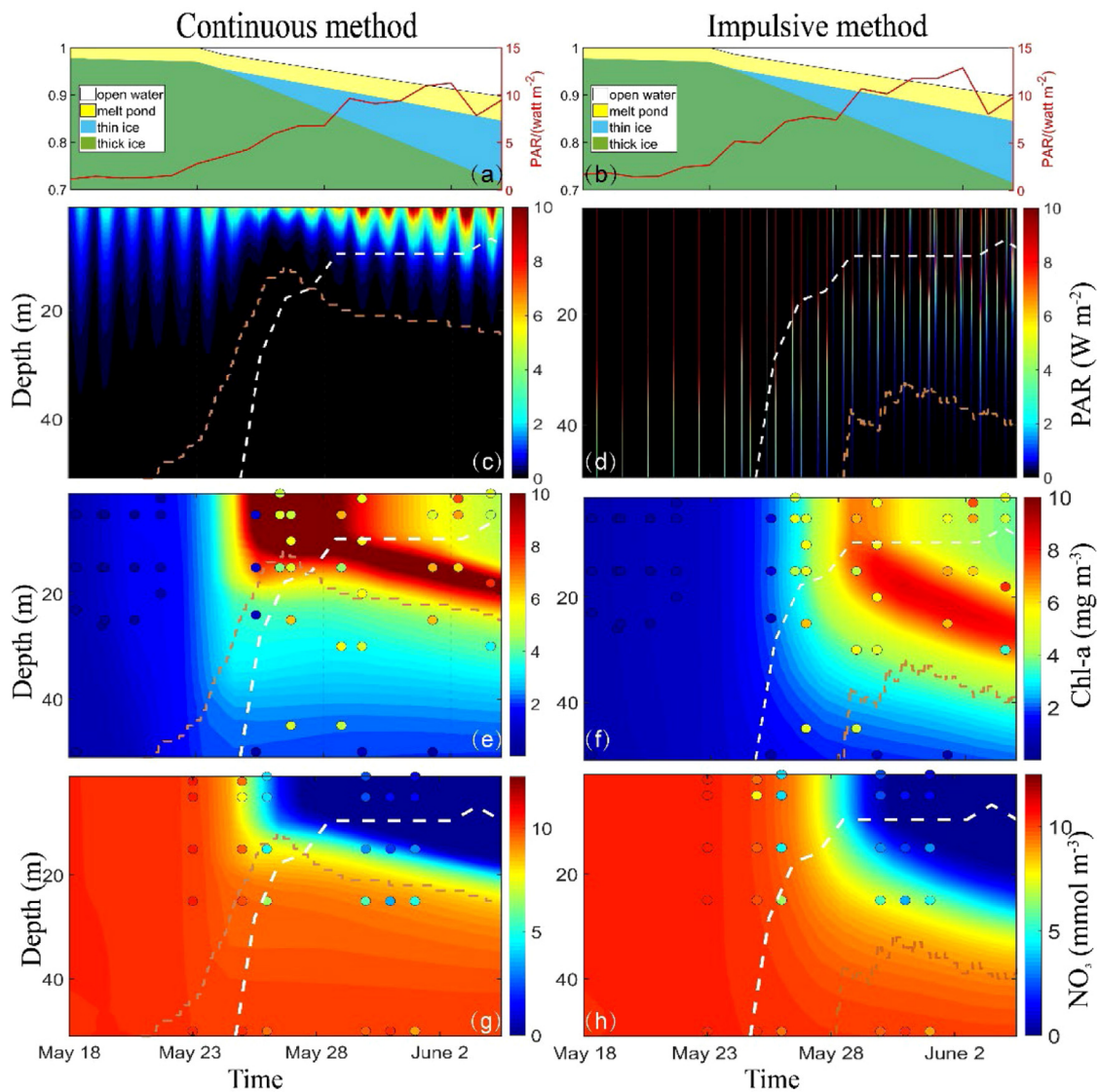
Fig. 6. (a) and (b) The daily fractions of the four different surface types (colored areas) and the daily PAR at sea surface (red line, W m^{-2}), (c) and (d) PAR profiles for the CRFS and the IRFS cases (W m^{-2}), (e) and (f) Modeled Chl-a for the CRFS and IRFS cases (mg m^{-3}), (g) and (h) Modeled NO$_3$ for the CRFS and IRFS cases (mmol m^{-3}). Note: The white dashed lines in (c)–(h) show the mixed layer depth, and the orange dashed lines show the euphotic depth. Colored circles denote the observational data. Sea ice and melt pond concentration data are from Assmy et al. (2017) and ICDC (http://icdc.zmaw.de), respectively.

until the end of simulation. When the bloom reaches peak value, the light limitation index decreases sharply in the vertical direction, especially under 20 m depth (Figs. 6c and 8b). As a result, the light limitation index for the CRFS case is much higher than that for the IRFS case near the surface (blue area above the solid black line in Fig. 8c), while it is evidently lower in the deeper layer (red area below the solid black line in Fig. 8c). From May 24th, the positive difference increases below the black line and reaches a positive peak on May 27th (Fig. 8c), which is related to earlier and overestimated bloom in the CRFS case. The IRFS allows more PAR to intermittently penetrate through the upper water column and supports the phytoplankton growth in the deeper part (10–40 m). Meanwhile, the CRFS confine the bloom to the surface layer (<15 m). Massive phytoplankton biomass accumulating near the surface, further prevents PAR from reaching the deep water (Pavlov et al., 2017), leading to the lower Chl-a concentration in deeper levels. In both cases, the nutrient limitation index keeps near 1.0 at the first five days and then decreases with the phytoplankton increase, which vertically forms a nutricline (Fig. 8d and e). The major differences between Fig. 8d and e are the depth of the nutricline and the time when the nutrients in the upper 10 m depth are depleted. There is a positive

peak at near surface from May 26th to 28th in Fig. 8f, which is because the earlier phytoplankton bloom leads to earlier nitrate depletion in the CRFS case than in the IRFS. The maximal negative difference between 10–30 m from May 29th in Fig. 8f indicates the lower boundary of the phytoplankton bloom and the deeper SCM in the IRFS case than in the other case. In addition, the phytoplankton net growth rates of these two cases are quite different. As shown in Fig. 8g, the Chl-a concentration increment in the IRFS case, which is less than 0.1 mg m^{-3} day^{-1}, can be neglected until May 23rd. In contrast, the net growth of phytoplankton Chl-a in the CRFS case gradually increases since simulation starts and reaches the peak on May 24th within a shallower depth (Fig. 8h). Thus, the difference of net growth between these two cases is negative initially and then reaches the minimum value when the bloom develops fastest at the surface layer in the CRFS case (Fig. 8i). Soon afterward, the positive maximum difference appears in the water column from the sea surface to the depth of 22 m. Note that, above 8.2 m, this maximum difference is due to nutrient limitation, while below this depth, the maximum difference is because of light limitation. Fig. 8 shows the definite discrepancies of the phytoplankton growth process between these two models.
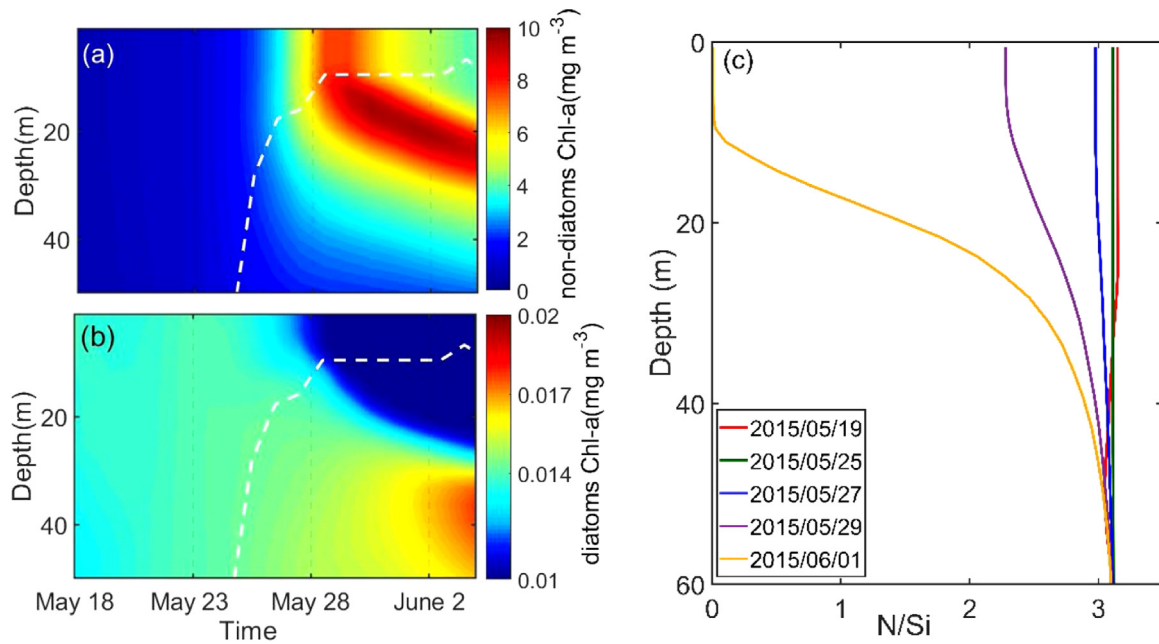
Fig. 7. Simulated Chl-a with the IRFS for (a) non-diatoms (mg m^{-3}) and (b) diatoms (mg m^{-3}), and (c) the molar ratio of N/Si in the simulation with the IRFS. Note: The white dashed lines in (a), (b) indicate the depth of the mixing layer.
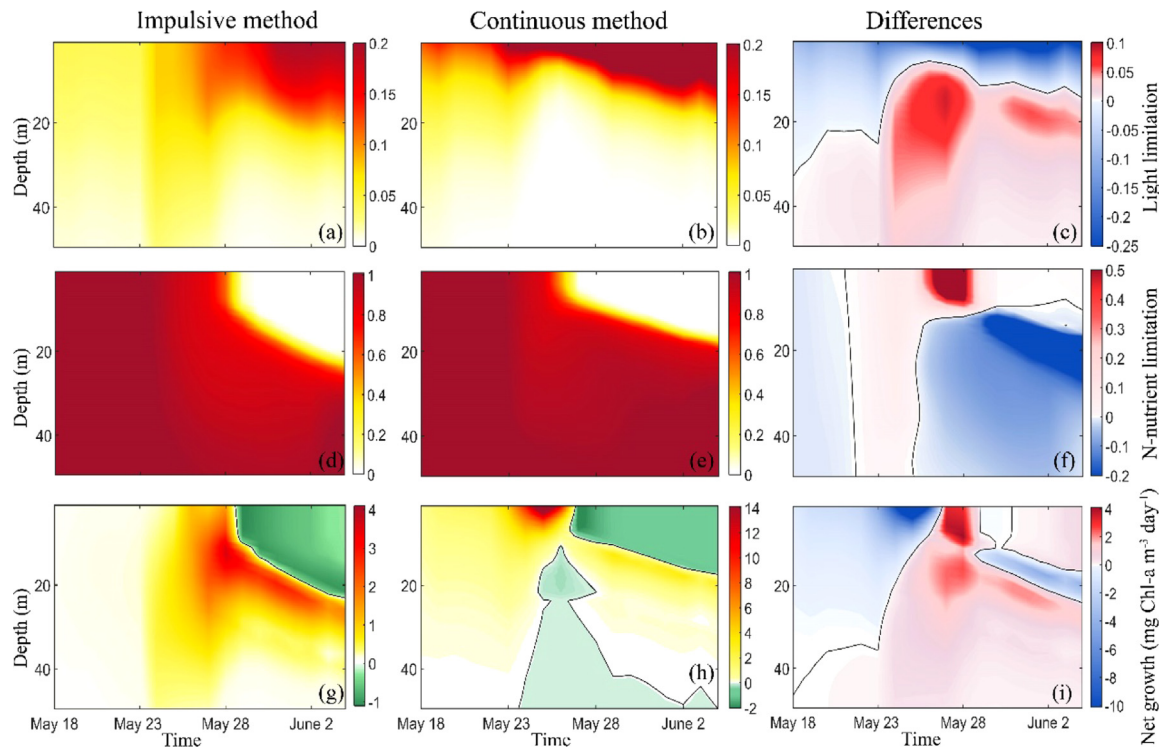

Fig. 8. The daily averaged light limitation indexes (first row), nitrogen limitation indexes (N-nutrient limitation, second row), and net growths of Chl-a (mg m^{-3} day^{-1}) (third row) for the IRFS case (left column), the CRFS case (middle column), and the differences between them (right column). Note: A higher value of the limitation index means a weaker limitation on the growth. The black lines in (e)–(i) denote the zero isoline. Note that colormap scale of subplots (a), (b) and (d), (e) are different.

For both IRFS and CRFS cases, an instantaneous light intensity of 0.016 W m^{-2} can support *Phaeocystis* net growth when nutrients are plentiful. Note that this value is lower than the threshold values reported for Arctic diatom blooms (Wang et al., 2014; Hill et al., 2018). It implies the competitive advantage for low light conditions of *Phaeocystis* than diatoms. For the CRFS case, surface PAR is calculated by the weighted average of the PAR transmitted through different surface types and stays higher than the threshold all day. Thus, a

bloom develops earlier with the net growth of Chl-a exceeding 1 mg m^{-3} day^{-1} by the second day (Fig. 8h). As shown in Eq. (6), the relationship between PAR and phytoplankton growth is inherently non-linear so that the CRFS produces an overestimation of phytoplankton growth at surface, though it is under high-concentration sea ice floe. For the IRFS case, because it generates an impulsive PAR field in the water column, phytoplankton growth shows an impulsive pattern correspondingly. Under the thick ice, solar radiation is attenuated to
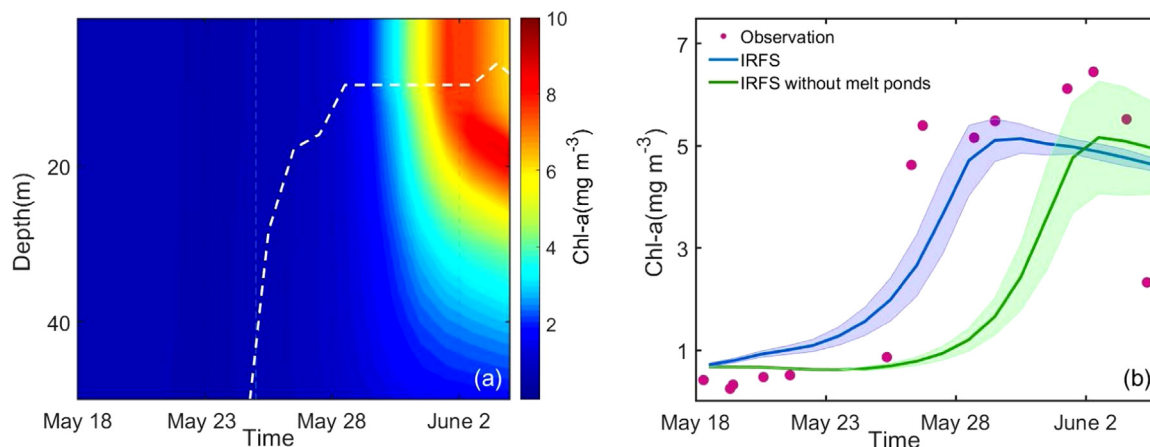
Fig. 9. (a) Vertical profile of simulated Chl-a with the IRFS without melt ponds (mg m^{-3}), (b) comparison of the averaged Chl-a in the upper 50 m between model runs with and without melt ponds. Note: The white dashed line in (a) indicates the depth of the mixed layer, and the shaded areas in (b) represent 3-fold standard deviations.

so extremely low value (<0.016 W m^{-2}) that can hardly support net phytoplankton growth. Therefore, phytoplankton Chl-a may increase only in open water or under melt ponds, while barely increasing under thick ice (Arrigo et al., 2014; Hill et al., 2018). Before May 24th, the water column is covered by thick ice with thick snow for most of the day (>99% sea ice concentration excluding ponded ice, Fig. 6b). Net phytoplankton growth (<2.5 mg m^{-3} day^{-1}) accumulates during the ephemeral melt ponds/open water conditions. But these accumulated phytoplankton Chl-a will be completely consumed by self-mortality and respiration during the thick ice periods. Therefore, the bloom cannot start until May 24th when the daily net growth becomes positive with the decrease of thick ice fraction (Fig. 8g).

To sum up, in this study, the bloom is triggered by the increasing PAR availability under a nutrient-sufficient condition. The IRFS approach provides a more accurate averaging of the light field. Production does not scale linearly with light. Therefore, light averaging prior to calculating production is mathematically inaccurate and thus produce inaccurate phytoplankton bloom. When the bloom is progressing, nutrients are reduced by phytoplankton growth, and are rarely replenished (much lower than the nitrate uptake) from deeper water column due to shallow pycnocline and low mixing rates (Randelhoff et al., 2016). It results in a nearly nitrate-depleted surface layer. Afterward, the surface bloom becomes nitrate-limited primarily (Fig. 8d and e). Additionally, grazing pressure may be an important factor regulating bloom development (Campbell et al., 2009; Lee et al., 2016). However, in the present study, low grazing on *Phaeocystis* is simulated (not shown), and this result is supported by the finding that *Phaeocystis* is considered unpalatable for the dominant *Calanus* species (Ray et al., 2016; Hop et al., 2021).

3.5. Impact of melt ponds on the model performance

Melt ponds are important for UIBs to develop, as they act like windows into the ocean and transmit 3–10 times more light than bare ice of the same thickness (Frey et al., 2011; Arrigo et al., 2014; Palmer et al., 2014). In the present study, the Case 3 using the IRFS without melt ponds is carried out to examine the impact of melt ponds. Simulation results show that this run can also reproduce the bloom process, but Chl-a concentration exceeds the bloom threshold (2.5 mg m^{-3}) only by May 30th, which is four days later than the experiment with melt pond fraction from satellite (Fig. 9a). Averaged Chl-a concentrations in the upper 50 m water column of the model runs with/without melt ponds are shown in Fig. 9b. For the run with melt ponds, the averaged Chl-a reaches the peak value three days earlier (May 30th vs. June 2nd) than in the no-melt ponds run. However, the maximum averaged Chl-a value does not change significantly (Fig. 9b). This result agrees well with a

previous study which indicated that doubling light intensity promotes an earlier bloom (Jin et al., 2006). On the day of the peak surface Chl-a concentration, the vertical extent of blooms in these two runs is 39.4 m. Melt pond coverage affects the progress of the phytoplankton bloom, such as changes in the bloom initiation and peak timing, but has little influence on bloom magnitude and depth. It is worth mentioning that this finding supports the results of Hill et al. (2018) that 7 days simulated delay in melt ponds postponed the onset of phytoplankton growth but did not impact the maximum biomass. This may essentially relate to the nutrient availability, Lavoie et al. (2009) showed that the amount of nutrients available at the end of the winter could be the determining factor of the spring UIB magnitude. Palmer et al. (2014) also suggested that UIBs are most likely to develop beneath sea ice with >10% melt pond coverage. However, it should be noted that their experiments did not include melt pond fraction between zero to 10%. The results of the present study show that even a smaller fraction of ponded area than 10% can affect the occurrence of a UIB.

4. Conclusions

The 1D ROMS-CoSiNE model has been upgraded to adapt to the mix-type ice-cover condition in the Arctic Ocean by proposing a new impulsive radiative forcing scheme. The impulsive radiative forcing scheme allows a random appearance of all ice conditions according to their areal fraction. The model reproduces the temporal evolution of an under-ice bloom in 2015 north of Svalbard, which was observed during the N-ICE2015 expedition. Ensemble runs show that the diurnal sequence of sea ice conditions does not influence the simulation results significantly. Compared with the widely used continuous radiative forcing scheme, the impulsive radiative forcing scheme performs better with lower biases, higher correlation coefficient and lower RMSD, especially near the surface layer of the water column (0–15 m). The simulation result of the continuous radiative case shows an earlier start of the bloom than observations and aggregation of Chl-a near the surface. In contrast, the simulation results of the impulsive radiative case agree well with observations, and a deeper and later phytoplankton bloom and corresponding deepened subsurface chlorophyll maxima are also simulated. The peak chlorophyll concentration of the impulsive radiative scheme is similar to observed data, while that of the continuous radiative scheme is two times higher than observed data. Moreover, sensitivity experiments with/without melt pond cover in the impulsive radiative forcing scheme show that the introduction of melt ponds produces the bloom four days earlier but does not change the magnitude of Chl-a concentration significantly. It indicates the important role of melt ponds in modulating the bloom timing.

This model is set to run under a Lagrangian coordinate, providing an approach for understanding the controlling process of observed

Table A.1
List of acronyms used.

Acronym	Definition
BIOMAS	Biology/Ice/Ocean Modeling and Assimilation System
CRFS	Continuous radiative forcing scheme
ECMWF	European Centre for Medium-Range Weather Forecasts
ICDC	Integrated Climate Data Center
ICESCAPE	Impacts of Climate on Ecosystems and Chemistry of the Arctic Pacific Environment
IRFS	Impulsive radiative forcing scheme
N-ICE2015	Norwegian young sea ICE experiment
NSIDC	National Snow and Ice Data Center
r	Correlation coefficient
PAR	Photosynthetically active radiation
RMSD	Root-mean-square difference
ROMS-CoSiNE	Regional Ocean Modeling System-Carbon Silicate Nitrate Ecosystem
SCM	Subsurface chlorophyll maxima
SD	Standard deviation
UIB	Under-ice phytoplankton bloom

Table B.2
Values and units for parameters used in the model.

Symbols	Descriptions	Values	Units	Reference
Alb_s	Thin/thick snow and melt ponds albedo for light	0.78/0.89/0.251	nondim	(5), (8)
k_s	Extinction coefficient in thin/thick snow	8.98/10.69	1/m	(2)
k_{ice}	Extinction coefficient in thin/thick ice and melt ponds	3.25/0.79/0.645	1/m	(2), (5)
$I0_{ice}$	Fraction of radiation transmitted through the highly scattering surface of thick/thin ice and melt ponds	0.93/0.97/0.99	nondim	(5)
$\alpha s1$	Initial slope of P–I curve of P1	0.93	1/(W/m^2)/day	(1)
$\alpha s2$	Initial slope of P–I curve of P2	0.25	1/(W/m^2)/day	(9)
$\mu1_{max}$	Maximum specific growth rate of P1	10.09	1/day	(1)
$\mu2_{max}$	Maximum specific growth rate of P2	1.44	1/day	(1)
$G1_{max}$	Maximum grazing rate by Z1	0.5	1/day	(10)
$G2_{max}$	Maximum grazing rate by Z2	0.25	1/day	(10)
$K1_{gr}$	Half saturation constant for Z1 grazing	1.0	mmol N/m^3	(7)
$K2_{gr}$	Half saturation constant for Z2 grazing	0.25	mmol N/m^3	(3)
$\psi1$	NH$_4$ inhibition parameter for P1	1.5	mmol N/m^3	(4)
$\psi1$	NH$_4$ inhibition parameter for P2	1.0	mmol N/m^3	(10)
K_{P1_NO3}	Half-saturation for NO$_3$ uptake by P1	1.0	mmol N/ m^3	(9)
K_{P2_NO3}	Half-saturation for NO$_3$ uptake by P2	1.0	mmol N/m^3	(7)
K_{P1_NH4}	Half-saturation for NH$_4$ uptake by P1	0.3	mmol N/m^3	(6)
K_{P2_NH4}	Half-saturation for NH$_4$ uptake by P2	1.0	mmol N/m^3	(3)
K_{P2_SiO4}	Half-saturation for SiO$_4$ uptake by P2	1.15	mmol Si/ m^3	(10)
$\gamma0$	Mesozooplankton specific mortality rate	0.035	1/day	(7)
$\gamma1$	Grazing efficiency of Z1	0.75	nondim	(6)
$\gamma2$	Grazing efficiency of Z2	0.75	nondim	(6)
$\gamma3$	P1 mortality	0.0585	1/day	(10)
$\gamma4$	P2 mortality	0.01	1/day	(6)
$\gamma6$	Aggregates rate	0.02	1/day	(6)
$\gamma7$	Nitrification rate	0.05	1/day	(9)
W1	Sinking velocity of P2 and Chl2	1	m/day	(3)
W2	Sinking velocity of detritus	10	m/day	(3)
W3	Sinking velocity of bSiO$_2$	60	m/day	(6)
R_{SiN}	Ratio of Si to N	1.5	mol Si/mol N	(3)
R_{PN}	Ratio of P to N	0.0625	mol P/mol N	(3), (9)
R_{CN}	Ratio of C to N	6.625	mol C/mol N	(3), (6)
R_{O2NO3}	Ratio of O$_2$ to NO$_3$	8.625	mol O$_2$/mol NO$_3$	(6), (9)
R_{O2NH4}	Ratio of O$_2$ to NH$_4$	6.625	mol O_2/mol NH$_4$	(6), (9)
$\rho1$	Z2 grazing preference for P2	0.70	nondim	(3)
$\rho2$	Z2 grazing preference for Z1	0.2	nondim	(3)
$\rho3$	Z2 grazing preference for detritus	0.1	nondim	(3)

(1) Assmy et al. (2017); (2) Calculated from observation; (3) Chai et al. (2002); (4) Fujii et al. (2007); (5) Light et al. (2008); (6) Ma et al. (2019); (7) Mortenson et al. (2017); (8) Taskjelle et al. (2017); (9) Xiu and Chai (2014); (10) Zhang et al. (2010).

ecological events during the expeditions as N-ICE2015. As Arctic sea ice is becoming younger, thinner, and more fragmented with more leads and melt ponds (Schourup-Kristensen et al., 2018), the IRFS provides valuable insights into the treatment of heterogeneous sea ice surface in under-ice biogeochemical simulations in a sub-grid scale. The 1D column can represent one grid cell in a 3D model and provides a tool for parameterization development (Mortenson et al., 2017). This work is intended as a step to implement an improved radiative forcing scheme in the Pan-Arctic model case.

CRediT authorship contribution statement

Yuexin Gao: Methodology, Writing – original draft, Visualization, Validation, Formal analysis, Data curation. **Yang Zhang:** Resources, Methodology, Software, Writing – review & editing. **Fei Chai:** Conceptualization, Program administration, Supervision, Funding acquisition. **Mats A. Granskog:** Resources, Validation, Writing – review & editing. **Pedro Duarte:** Methodology, Writing – review & editing. **Philipp Assmy:** Investigation, Writing – review & editing.

Declaration of competing interest

The authors declare that they have no known competing financial interests or personal relationships that could have appeared to influence the work reported in this paper.

Acknowledgments

Appendix A

See Table A.1.

Appendix B

See Table B.2.

References

Andersen, O.G.N., 1989. Primary production, chlorophyll, light, and nutrients beneath the Arctic sea ice. In: Herman, Y. (Ed.), The Arctic Seas. Von Nostrand Reinhold, pp. 147–191.

Ardyna, M., Mundy, C.J., Mayot, N., Matthes, L.C., Oziel, L., Horvat, C., Leu, E., Assmy, P., Hill, V., Matrai, P.A., Gale, M., Melnikov, I.A., Arrigo, K.R., 2020b. Under-ice phytoplankton blooms: Shedding light on the invisible part of arctic primary production. Front. Mar. Sci. 7, 608032. http://dx.doi.org/10.3389/fmars.2020.608032.

Ardyna, M., Mundy, C.J., Mills, M.M., Oziel, L., Grondin, P.L., Lacour, L., Verin, G., Dijken, G.L., Ras, J., Alou-Font, E., Babin, M., Gosselin, M., Tremblay, J.E., Raimbault, P., Assmy, P., Nicolaus, M., Claustre, H., Arrigo, K.R., 2020a. Environmental drivers of under-ice phytoplankton bloom dynamics in the Arctic Ocean. Elementa Sci. Anthr. 8, 30. http://dx.doi.org/10.1525/elementa.430.

Arrigo, K.R., van Dijken, G.L., 2015. Continued increases in Arctic Ocean primary production. Prog. Oceanogr. 136, 60–70. http://dx.doi.org/10.1016/j.pocean.2015.05.002.

Arrigo, K.R., Perovich, D.K., Pickart, R.S., Brown, Z.W., van Dijken, G.L., Lowry, K.E., Mills, M.M., Palmer, M.A., Balch, W.M., Bahr, F., Bates, N.R., Benitez-Nelson, C., Bowler, B., Brownlee, E., Ehn, J.K., Frey, K.E., Garley, R., Laney, S.R., Lubelczyk, L., Mathis, J., Matsuoka, A., Mitchell, B.G., Moore, G.W.K., Ortega-Retuerta, E., Pal, S., Polashenski, C.M., Reynolds, R.A., Scheiber, B., Sosik, H.M., Stephens, M., Swift, J.H., 2012. Massive phytoplankton blooms under Arctic sea ice. Science 336, 1408. http://dx.doi.org/10.1126/science.1215065.

Arrigo, K.R., Perovich, D.K., Pickart, R.S., Brown, Z.W., van Dijken, G.L., Lowry, K.E., Mills, M.M., Palmer, M.A., Balch, W.M., Bates, N.R., Benitez-Nelson, C.R., Brownlee, E., Frey, K.E., Laney, S.R., Mathis, J., Matsuoka, A., Mitchell, B.G., Moore, G.W.K., Reynolds, R.A., Sosik, H.M., Swift, J.H., 2014. Phytoplankton blooms beneath the sea ice in the Chukchi sea. Deep Sea Res. II http://dx.doi.org/10.1016/j.dsr2.2014.03.018.

[Dataset], Assmy, P., Duarte, P., Dujardin, J., Fernández-Méndez, M., Fransson, A., Hodgson, Kauko, H., Kristiansen, S., Mundy, C.J., Olsen, L.M., Peeken, I., Sandbu, M., Wallenschus, J., Wold, A., 2016. N-ICE2015 Water Column Biogeochemistry. Norwegian Polar Institute, http://dx.doi.org/10.21334/npolar.2016.3ebb7f64.

Assmy, P., Fernández-Méndez, M., Duarte, P., Meyer, A., Randelhoff, A., Mundy, C.J., 2017. Leads in Arctic pack ice enable early phytoplankton blooms below snow-covered sea ice. Sci. Rep. 7, 40850. http://dx.doi.org/10.1038/srep40850.

Campbell, R.G., Sherr, E.B., Ashjian, C.J., Plourde, S., Sherr, B.F., Hill, V., Stockwell, D.A., 2009. Mesozooplankton prey preference and grazing impact in the western Arctic Ocean. Deep Sea Res. II 56, 1274–1289. http://dx.doi.org/10.1016/j.dsr2.2008.10.027.

Castellani, G., Veyssière, G., Karcher, M., Stroeve, J., Banas, S.N., Bouman, A.H., Brierley, S.A., Connan, S., Cottire, F., Groze, F., Hobbs, L., Katlein, C., Light, B., McKee, D., Orkney, A., Proud, R., Schourup-Kristensen, V., 2022. Shine a light: Under-ice light and its ecological implications in a changing Arctic Ocean. Ambio 51, 307–317. http://dx.doi.org/10.1007/s13280-021-01662-3.

Chai, F., Dugdale, R.C., Peng, T.-H., Wilkerson, F.P., Wilkerson, Barber, R.T., 2002. One-dimensional ecosystem model of the equatorial Pacific upwelling system. Part I: model development and silicon and nitrogen cycle. Deep Sea Res. II 49 (13–14), 2713–2745. http://dx.doi.org/10.1016/S0967-0645(02)00055-3.

Clement Kinney, J., Maslowski, W., Osinski, R., Jin, M., Frants, M., Jeffery, N., Lee, Y.J., 2020. Hidden production: On the importance of pelagic phytoplankton blooms beneath Arctic Sea ice. J. Geophys. Res. Oceans 125, e2020JC016211. http://dx.doi.org/10.1029/2020JC016211.

Cota, G.F., Smith, Jr., W.O., Mitchell, B.G., 1994. Photosynthesis of *Phaeocystis* in the Greenland Sea. Limnol. Oceanogr. 39, 948–953. http://dx.doi.org/10.4319/lo.1994.39.4.0948.

Degerlund, M., Eilertsen, H.C., 2010. Main species characteristics of phytoplankton spring blooms in NE Atlantic and Arctic Waters (68–80 degrees N). Estuar. Coasts 33, 242–269. http://dx.doi.org/10.1007/s12237-009-9167-7.

[Dataset], Dodd, P.A., Meyer, A., Fransson, A., Duarte, P., Koenig, Z., Cooper, A., Smedsrud, L.H., Hendry, K., Rerolle, V., Silyakova, A., Kusse-Tiuz, N., Miguet, J., Davis, P., 2016. N-ICE2015 Bottle Data from Ship Water Sampler. Norwegian Polar Institute, http://dx.doi.org/10.21334/npolar.2016516bc529.

Duarte, P., Assmy, P., Hop, H., Spreen, G., Gerland, S., Hudson, S.R., 2015. The importance of vertical resolution in sea ice algae production models. J. Mar. Syst. 145, 69–90. http://dx.doi.org/10.1016/j.jmarsys.2014.12.004.

Frants, M., Maslowski, W., Osinski, R., Jeffery, N., Jin, M., Clement Kinney, J., 2020. Evaluation of under sea-ice phytoplankton blooms in the fully-coupled, high-resolution regional arctic system model (RASM). http://dx.doi.org/10.1002/essoar.10503749.1, Preprint.

Frey, K.E., Perovich, D.K., Light, B., 2011. The spatial distribution of solar radiation under a melting Arctic sea ice cover. Geophys. Res. Lett. 38, L22501. http://dx.doi.org/10.1029/2011GL049421.

Fujii, M., Boss, E., Chai, F., 2007. The value of adding optics to ecosystem models: a case study. Biogeosciences 4, 817–835. http://dx.doi.org/10.5194/bg-4-817-2007.

Gosselin, M., Levasseur, M., Wheeler, P.E., Horner, R.A., Booth, B.C., 1997. New measurements of phytoplankton and ice algal production in the Arctic Ocean. Deep Sea Res. II 44, 1623–1644. http://dx.doi.org/10.1016/S0967-0645(97)00054-4.

Granskog, M.A., Assmy, P., Gerland, S., Spreen, G., Steen, H., Smedsrud, L.H., 2016. Arctic research on thin ice: consequences of Arctic sea ice loss. Eos. Trans. AGU 97, 22–26. http://dx.doi.org/10.1029/2016EO044097.

Granskog, M.A., Fer, I., Rinke, A., Steen, H., 2018. Atmosphere-ice-ocean-ecosystem processes in a thinner arctic sea ice regime: The Norwegian young sea ice (N-ICE2015) expedition. J. Geophys. Res. Oceans 123, http://dx.doi.org/10.1002/2017JC013328.

Hill, V., Cota, G., 2005. Spatial patterns of primary production on the shelf, slope and basin of the Western Arctic in 2002. Deep Sea Res. II 52, 3344–3354. http://dx.doi.org/10.1016/j.dsr2.2005.10.001.

Hill, V.J., Light, B., Steele, M., Zimmerman, R.C., 2018. Light availability and phytoplankton growth beneath Arctic sea ice: Integrating observations and modeling. J. Geophys. Res. Oceans 123, http://dx.doi.org/10.1029/2017JC013617.

Hop, H., Wold, A., Meyer, A., Bailey, A., Hatlebakk, M., Kwasniewski, S., Leopold, P., Kuklinski, P., Søreide, J.E., 2021. Winter-spring development of the zooplankton community below sea ice in the Arctic Ocean. Front. Mar. Sci. 8, 609480. http://dx.doi.org/10.3389/fmars.2021.609480.

Horvat, C., Jones, D.-R., Iams, S., Schroeder, D., Flocco, D., Feltham, D., 2017. The frequency and extent of sub-ice phytoplankton blooms in the Arctic Ocean. Sci. Adv. 3, e1601191. http://dx.doi.org/10.1126/sciadv.1601191.

Istomina, L., Heygster, G., Huntemann, M., Schwarz, P., Birnbaum, G., Scharien, R., Polashenski, C., Perovich, D., Zege, E., Malinka, A., Prikhach, A., Katsev, I., 2015. Melt pond fraction and spectral sea ice albedo retrieval from MERIS data – Part 1: Validation against in situ, aerial, and ship cruise data. Cryosphere 9, 1551–1566. http://dx.doi.org/10.5194/tc-9-1551-2015.

Itkin, P., Spreen, G., Cheng, B., Doble, M., Girard-Ardhuin, F., Haapala, J., Hughes, N., Kaleschke, L., Nicolaus, M., Wilkinson, J., 2017. Thin ice and storms: Sea ice deformation from buoy arrays deployed during N-ICE2015. J. Geophys. Res. Oceans 122, 4661–4674. http://dx.doi.org/10.1002/2016JC012403.

Jin, M., Deal, C.J., Wang, J., Tanaka, N., Ikeda, M., 2006. Vertical mixing effects on the phytoplankton bloom in the southeastern Bering Sea midshelf. J. Geophys. Res. 111, C03002. http://dx.doi.org/10.1029/2005JC002994.

Jin, M., Popova, E.E., Zhang, J., Ji, R., Pendleton, D., Varpe, Ø., Yool, A., Lee, Y.J., 2016. Ecosystem model intercomparison of under-ice and total primary production in the Arctic Ocean. J. Geophys. Res. Oceans 121, http://dx.doi.org/10.1002/2015JC011183.

Johnsen, G., Norli, M., Moline, M., Robbins, I., Quillfeldt, C., Sørnsen, K., Cottier, F., Berge, J., 2018. The advective origin of an under-ice spring bloom in the Arctic Ocean using multiple observational platforms. Polar Biol. http://dx.doi.org/10.1007/s00300-018-2278-5, online.

King, J., Spreen, G., Gerland, S., Haas, C., Hendriks, S., Kaleschke, L., Wang, C., 2018. Sea-ice thickness from field measurements in the northwestern Barents Sea. J. Geophys. Res. Oceans 122, 1497–1512. http://dx.doi.org/10.1002/2016J012199.

Kwok, R., Rothrock, D.A., 2009. Decline in Arctic sea ice thickness from submarine and ICESat records: 1958–2008. Geophys. Res. Lett. 36, L15501. http://dx.doi.org/10.1029/2009GL039035.

Laufkötter, C., Vogt, M., Gruber, N., Aita-Noguchi, M., Aumont, O., Bopp, L., Buitenhuis, E., Doney, S.C., Dunne, J., Hashioka, T., 2015. Drivers and uncertainties of future global marine primary production in marine ecosystem models. Biogeosciences 12, 6955–6984. http://dx.doi.org/10.5194/bg-12-6955-2015.

Lavoie, D., Macdonald, R.W., Denman, K.L., 2009. Primary productivity and export fluxes on the Canadian shelf of the Beaufort Sea: A modelling study. J. Mar. Syst. 75 (1–2), 17–32. http://dx.doi.org/10.1016/j.jmarsys.2008.07.007.

Lee, Y.J., Matrai, P.A., Friedrichs, M.A.M., Saba, V.S., Aumont, O., Babin, M., Buitenhuis, E.T., 2016. Net primary productivity estimates and environmental variables in the Arctic Ocean: An assessment of coupled physical-biogeochemical models. J. Geophys. Res. Oceans 121, 12. http://dx.doi.org/10.1002/2016JC011993.

Lee, S.H., Whitledge, T.E., 2005. Primary and new production in the deep Canada Basin during summer 2002. Polar Biol. 28, 190–197. http://dx.doi.org/10.1007/s00300-004-0676-3.

Lewis, K.M., Arntsen, A.E., Coupel, P., Joy-Warren, H., Lowry, K.E., Mastsuoka, A., Mills, M.M., Dijken, G.L., Selz, V., Arrigo, K.R., 2018. Photoacclimation of Arctic Ocean phytoplankton to shifting light and nutrient limitation. Limnol. Oceanogr. 9999, 1–18. http://dx.doi.org/10.1002/lno.11039.

Light, B., Grenfell, T.C., Perovich, D.K., 2008. Transmission and absorption of solar radiation by Arctic sea ice during the melt season. J. Geophys. Res. 113, C03023. http://dx.doi.org/10.1029/2006JC003977.

Lowry, K.E., van Dijken, G.L., Arrigo, K.R., 2014. Evidence of under-ice phytoplankton blooms in the Chukchi Sea from 1998 to 2012. Deep Sea Res. II 105, 105–117. http://dx.doi.org/10.1016/j.dsr2.2015.06.006.

Lowry, K.E., Pickart, R.S., Selz, V., Mills, M.M., Pacini, A., Lewis, K.M., Arrigo, K.R., 2018. Under-ice phytoplankton blooms inhibited by spring convective mixing in refreezing leads. J. Geophys. Res. Oceans 123, 90–109. http://dx.doi.org/10.1002/2016JC012575.

Ma, W., Xiu, P., Chai, F., Li, H., 2019. Seasonal variability of the carbon export in the central South China Sea. Ocean Dyn. http://dx.doi.org/10.1007/s10236-019-01286-y, online.

Maslanik, J., Stroeve, J., Fowler, C., Emery, W., 2011. Distribution and trends in Arctic sea ice age through spring 2011. Geophys. Res. Lett. 38, L13502. http://dx.doi.org/10.1029/2011GL047735.

Massicotte, P., Peeken, I., Katlein, C., Flores, H., Huot, Y., Castellani, G., Arndt, S., Lange, B.A., Tremblay, J.-É., Babin, M., 2019. Sensitivity of phytoplankton primary production estimates to available irradiance under heterogeneous sea ice conditions. J. Geophys. Res. Oceans 124, 5436–5450. http://dx.doi.org/10.1029/2019jc015007.

Meyer, A., Sundfjord, A., Fer, I., Provost, C., Robineau, N.V., Koenig, Z., Onarheim, I.H., Smedrud, L.H., Duarte, P., Dodd, P.A., Graham, R.M., Schmidtko, S., Kauko, H.M., 2017. Winter to summer oceanographic observations in the Arctic Ocean north of Svalbard. J. Geophys. Res. Oceans 122, 6218–6237. http://dx.doi.org/10.1002/2016JC012391.

Mortenson, E., Hayshida, H., Steiner, N., Monahan, A., Blais, M., Gale, M.A., Galindo, V., Gosselin, M., Hu, X., Lavoie, D., Mundy, C.J., 2017. A model-based analysis of physical and biological controls on ice algal and pelagic primary production in Resolute Passage. Elementa: Sci. Anthr. 5, 39. http://dx.doi.org/10.1525/elementa.229.

Mundy, C.J., Gosselin, M., Ehn, J., Gratton, Y., Rossnagel, A., Barber, D., Martin, J., Tremblay, J.-É., Palmer, M., Arrigo, K.R., Darnis, G., Fortier, L., Else, B., Papakyriakou, T., 2009. Contribution of under-ice primary production to an ice-edge upwelling phytoplankton bloom in the Canadian Beaufort Sea. Geophys. Res. Lett. 36, GL038837. http://dx.doi.org/10.1029/2009GL038837.

Mundy, C.J., Gosselin, M., Gratton, Y., Brown, K., Galindo, V., Campbell, K., et al., 2014. Role of environmental factors on phytoplankton bloom initiation under landfast sea ice in Resolute Passage, Canada. Mar. Ecol. Prog. Ser. 497, 39–49. http://dx.doi.org/10.3354/meps10587.

Oziel, L., Massicotte, P., Randelhoff, A., Ferland, J., Vladoiu, A., Lacour, L., Galindo, V., Lambert-Girard, S., Dumont, D., Cuypers, Y., Bouruet-Aubertot, P., Mundy, C.J., Ehn, J., Bécu, G., Marec, C., Forget, M.H., Garcia, N., Coupel, P., Raimbault, P., Houssais, M.N., Babin, M., 2019. Environmental factors influencing the seasonal dynamics of spring algal blooms in and beneath sea ice in western Baffin Bay. Elementa Sci. Anthr. 7 (1), 34. http://dx.doi.org/10.1525/elementa.372.

Palmer, M.A., Saenz, B.T., Arrigo, K.R., 2014. Impacts of sea ice retreat, thinning, and melt-pond proliferation on the summer phytoplankton bloom in the Chukchi Sea, Arctic Ocean. Deep Sea Res. II 105, 85–104. http://dx.doi.org/10.1016/j.dsr2.2014.03.016.

Pavlov, A.K., Taskjelle, T., Kauko, H.M., Hamre, B., Hudson, S.R., Assmy, P., Duarte, P., Fernández Méndez, M., Mundy, C.J., Granskog, M.A., 2017. Altered inherent optical properties and estimates of the underwater light field during an arctic under-ice bloom of *Phaeocystis pouchetii*. J. Geophys. Res. 122, 4939–4961. http://dx.doi.org/10.1002/2016JC012471.

Payne, C.M., Bianucci, L., can Dijken, G.L., Arrigo, K.R., 2021. Changes in under-ice primary production in the Chukchi Sea from 1988 to 2018. J. Geophys. Res. Oceans 126, e2021JC017483. http://dx.doi.org/10.1029/2021JC017483.

Perovich, D.K., 2005. On the aggregate-scale partitioning of solar radiation in Arctic sea ice during the Surface Heat Budget of the Arctic Ocean (SHEBA) field experiment. J. Geophys. Res. Oceans 110, C03002. http://dx.doi.org/10.1029/2004JC002512.

Polyakov, I.V., Walsh, J.E., Kwok, R., 2012. Recent changes of Arctic multiyear sea ice coverage and the likely causes. Bull. Am. Meteorol. Soc. 93 (2), 145–151. http://dx.doi.org/10.1175/BAMS-D-11-00070.1.

Popova, E.E., Yool, A., Coward, A.C., Aksenov, Y.K., Alderson, S.G., Cuecas, B.A., Anderson, T.R., 2010. Control of primary production in the Arctic by nutrients and light: insights from a high resolution ocean general circulation model. Biogeosci. Discuss. 7, 5557–5620. http://dx.doi.org/10.5194/bgd-7-5557-2010.

Randelhoff, A., Fer, I., Sundfjord, A., Tremblay, J.-É., Reigstad, M., 2016. Vertical fluxes of nitrate in the seasonal nitracline of the Atlantic sector of the Arctic Ocean. J. Geophys. Res. Oceans 121, 5282–5295. http://dx.doi.org/10.1002/2016JC011779.

Ray, J.L., Skaar, K.S., Simonelli, P., Larsen, A., Sazhin, A., Jakobsen, H.H., Nejstgaard, J.C., Troedsson, C., 2016. Molecular gut content analysis demonstrates that Calanus grazing on *Phaeocystis pouchetii* and *Skeletonema marinoi* is sensitive to bloom phase but not prey density. Mar. Ecol. Prog. Ser. 542, 63–77. http://dx.doi.org/10.3354/meps11560.

Rösel, A., Kaleschke, L., Birnbaum, G., 2012. Melt ponds on Arctic sea ice determined from MODIS satellite data using an artificial neural network. Cryosphere 6 (2), 431–446. http://dx.doi.org/10.5194/tc-6-431-2012.

[Dataset], Rösel, A., King, J., Kasajima, Y., 2017. N-ICE2015 Ice Thickness, Snow Thickness, and Freeboard from Thickness Drillings. Norwegian Polar Institute, http://dx.doi.org/10.21334/npolar.2017.25f70db1.

Sakshaug, E., Johnsen, G., Kristiansen, S., Quillfeldt, C.H., Rey, F., Slagstad, D., Thingstad, F., 2009. Phytoplankton and primary production. In: Sakshaug, E., Johnsen, G., Kovacs, K.M. (Eds.), Ecosystem Barents Sea. Tapir Academic Press, Trondheim, pp. 167–208.

Schourup-Kristensen, V., Wekerle, C., Danilov, S., Völker, C., 2021. Seasonality of mesoscale phytoplankton control in eastern Fram Strait. J. Geophys. Res. Oceans 126, e2021JC017279. http://dx.doi.org/10.1029/2021JC017279.

Schourup-Kristensen, V., Wekerle, C., Wolf-Gladrow, D.A., Völker, C., 2018. Arctic Ocean biogeochemistry in the high resolution FESOM 1.4-REcoM2 model. Prog. Oceanogr. 168, 65–81. http://dx.doi.org/10.1016/j.pocean.2018.09.006.

Simo-Matchim, A.G., Gosselin, M., Poulin, M., Ardyna, M., Lessard, S., 2017. Summer and fall distribution of phytoplankton in relation to environmental variables in labrador fjords, with special emphasis on *Phaeocystis pouchetii*. Mar. Ecol. Prog. Ser. 572 (May31), 19–42. http://dx.doi.org/10.3354/meps12125.

Slagstad, D., Støle-Hansen, K., 1991. Dynamics of plankton growth in the Barents Sea: model studies. Polar Res. 10 (1), 173–186. http://dx.doi.org/10.3402/polar.v10i1.6736.

Smith, W.O., Sakshaug, E., 1990. Polar phytoplankton. In: Smith, W.O. (Ed.), Polar Oceanography, Part B. Academic, San Diego, pp. 475–525.

Stroeve, J.C., Serreze, M.C., Holland, M.M., Kay, J.E., Maslanik, J., Barrett, A.P., 2012. The Arctic's rapidly shrinking sea ice cover: a research synthesis. Clim. Change 110 (3–4), 1005–1027. http://dx.doi.org/10.1007/s10584-011-0101-1.

Stroeve, J., Vancoppenolle, M., Veyssiere, G., Lebrun, M., Castellani, G., Babin, M., Karcher, M., Landy, J., Liston, G.E., Wilkinson, J., 2021. A multi-sensor and modeling approach for mapping light under sea ice during the ice-growth season. Front. Mar. Sci. 7, 592337. http://dx.doi.org/10.3389/fmars.2020.592337.

Taskjelle, T., Granskog, M.A., Pavlov, A.K., Hudson, S.R., Hamre, B., 2017. Effects of an Arctic under-ice bloom on solar radiant heating of the water column. J. Geophys. Res. Oceans 122, http://dx.doi.org/10.1002/2016JC012187.

[Dataset], Taskjelle, T., Hudson, S.R., Pavlov, A., Granskog, M.A., 2016. N-ICE2015 Surface and under-Ice Spectral Shortwave Radiation Data. Norwegian Polar Institute, http://dx.doi.org/10.21334/npolar.2016.9089792e.

Walsh, J.J., Dieterle, D.A., Maslowski, W., Whitledge, T.E., 2004. Decadal shifts in biophysical forcing of Arctic marine food webs: Numerical consequences. J. Geophys. Res. 109, C05031. http://dx.doi.org/10.1029/2003JC001945.

Wang, Q., Danilov, S., Jung, T., Kaleschke, L., Wernecke, A., 2016. Sea ice leads in the Arctic Ocean: Model assessment, interannual variability and trends. Geophys. Res. Lett. 43, 7019–7027. http://dx.doi.org/10.1002/2016GL068696.

Wang, C.X., Granskog, M.A., Gerland, S., Hudson, S.R., Perovich, D.K., Nicolaus, M., 2014. Autonomous observations of solar energy partitioning in first-year sea ice in the Arctic Basin. J. Geophys. Res. Oceans 119, 2066–2080. http://dx.doi.org/10.1002/2013JC009459.

Willmes, S., Heinemann, G., 2016. Sea-ice wintertime lead frequencies and regional characteristics in the Arctic 2003–2015. Remote Sens. 8, http://dx.doi.org/10.3390/rs8010004.

Xiu, P., Chai, F., 2011. Modeled biogeochemical responses to mesoscale eddies in the South China Sea. J. Geophys. Res. 116, C10006. http://dx.doi.org/10.1029/2010jc006800.

Xiu, P., Chai, F., 2014. Connections between physical, optical and biogeochemical processes in the Pacific Ocean. Prog. Oceanogr. 122, 30–53. http://dx.doi.org/10.1016/j.pocean.2013.11.008.

Zhang, J., Ashjian, C., Campbell, R., Spitz, Y.H., Steele, M., Hill, V., 2015. The influence of sea ice and snow cover and nutrient availability on the formation of massive under-ice phytoplankton blooms in the Chukchi Sea. Deep Sea Res. II 118, 122–135. http://dx.doi.org/10.1016/j.dsr2.2015.02.008.

Zhang, J., Spitz, Y.H., Steele, M., Ashjian, C., Campbell, R., Berline, L., Matrai, P., 2010. Modeling the impact of declining sea ice on the Arctic marine planktonic ecosystem. J. Geophys. Res. 115, C10015. http://dx.doi.org/10.1029/2009JC005387.

Further reading

Schlitzer, R., 2015, Ocean data view software package, version 5.2.0. Accessed at http://odv.awi.de.